INTERNATIONAL JOURNAL FOR NUMERICAL METHODS IN FLUIDS
Int. J. Numer. Meth. Fluids **28**: 541–563 (1998)

SHALLOW-WATER FLOW SOLVER WITH NON-HYDROSTATIC PRESSURE: 2D VERTICAL PLANE PROBLEMS

P.K. STANSBY* AND J.G. ZHOU

Hydrodynamics Research Group, Manchester School of Engineering, The University of Manchester, Manchester M13 9PL, UK

SUMMARY

A numerical solution for shallow-water flow is developed based on the unsteady Reynolds-averaged Navier–Stokes equations without the conventional assumption of hydrostatic pressure. Instead, the non-hydrostatic pressure component may be added in regions where its influence is significant, notably where bed slope is not small and separation in a vertical plane may occur or where the free-surface slope is not small. The equations are solved in the σ-co-ordinate system with semi-implicit time stepping and the eddy viscosity is calculated using the standard k–ϵ turbulence model. Conventionally, boundary conditions at the bed for shallow-water models only include vertical diffusion terms using wall functions, but here they are extended to include horizontal diffusion terms which can be significant when bed slope is not small. This is consistent with the inclusion of non-hydrostatic pressure. The model is applied to the 2D vertical plane flow of a current over a trench for which experimental data and other numerical results are available for comparison. Computations with and without non-hydrostatic pressure are compared for the same trench and for trenches with smaller side slopes, to test the range of validity of the conventional hydrostatic pressure assumption. The model is then applied to flow over a 2D mound and again the slope of the mound is reduced to assess the validity of the hydrostatic pressure assumption. © 1998 John Wiley & Sons, Ltd.

KEY WORDS: shallow-water flow; non-hydrostatic pressure; k–ϵ turbulence model; σ-co-ordinate

1. INTRODUCTION

The shallow-water equations in depth-averaged form have been successfully applied to many engineering problems and their use has become standard practice in environmental impact studies in estuarial and coastal regions. In many situations however, particularly those involving solute and sediment transport, the vertical variation of velocity is also important and 3D computations, maintaining the hydrostatic pressure assumption, have become a practical proposition with increasing computer power. The horizontal momentum and depth-integrated continuity equations are solved directly, incorporating some form of turbulence model. The vertical accelerations are required to be negligible and vertical velocity is approximated from the (local) continuity equation. In this paper the general solver of Stansby [1] is used as the starting point. This has a finite volume conservative formulation, implicit time stepping for

---

* Correspondence to: Manchester School of Engineering, Simon Building, The University of Manchester, Oxford Road, Manchester M13 9PL, UK.

CCC 0271–2091/98/130541–23$17.50

Received June 1997
Revised October 1997

vertical diffusion and surface elevation terms, and explicit time stepping for horizontal diffusion and source terms. The co-ordinate system is used to provide an accurate resolution at the bed and free surface, and the $k-\epsilon$ turbulence transport equation defines eddy viscosity. Other schemes are reviewed in Reference [1] and this will not be repeated here. In this paper, the aim is to develop the method in order to remove the limitation of the hydrostatic pressure assumption which requires small bed and free-surface slopes and, in particular, restricts separation at the bed in a vertical plane. Experiments with conical islands of small side slope (as small as 10°) have indicated that separation in a vertical plane does occur and has a significant influence on flow near the island [2]. Corresponding findings have been made for tidal flow around a headland [3]. In this paper, a method is presented which allows the non-hydrostatic pressure component to be computed in areas where its effect is significant, but omitted elsewhere. This is important for large-scale simulations, because the computation of non-hydrostatic pressure involves a time consuming Poisson-equation solution and it is desirable that the domain of solution is as restricted as possible. That such an approach may be contemplated at all is due to highly efficient equation solving methods. This is already used for the computation of surface elevation (in a horizontal plane) but is even more important for the solution of the pressure field (3D in general but 2D for the vertical plane problems considered here).

There is limited previous work on this problem. Johns [4] presented a method for 2D vertical-plane problems without directly solving the vertical momentum equation, but determined vertical velocity from local continuity and non-hydrostatic pressure from the integrated vertical momentum equation (in its steady state form) and iterated to a solution. The approach would thus appear to be limited to steady problems and its lack of direct horizontal and vertical coupling would suggest that it is not a robust general method. Nevertheless, the importance of non-hydrostatic pressure in sand-wave problems was demonstrated. Casulli and Stelling [5] incorporated non-hydrostatic pressure in the Cartesian scheme of Casulli and Cheng [6]. This showed some promising results but the influence of non-hydrostatic pressure on free-surface elevation was not included and the effect of horizontal diffusion at the bed where the slope is not small was not considered.

In this paper, a general and, it is believed, robust formulation based on the fractional step method is presented. Non-hydrostatic pressure is included in the momentum equations for incorporation in the surface elevation solution. Local continuity is then satisfied accurately at the end of a time step by adjusting pressures (and velocities) through the solution of a Poisson equation. The influence of horizontal diffusion at the bed is noted. The method is tested on the 2D vertical plane problem of current flow over a trench for which experimental data and other numerical results are available. The model is also applied to flow over a 2D hill for which experimental results may be inferred for subcritical free-surface flow. In both situations, the slopes are reduced to assess the accuracy of simulations without non-hydrostatic pressure.

2. 2D FLOW MODEL

The large-scale, slowly-varying structures of the flow are to be computed directly with the small-scale turbulent structures modelled using the Boussinesq eddy viscosity concept, which relates the time-averaged Reynolds stresses to the time-averaged velocity gradients. The averaging time is necessarily small in relation to the time scales of the large-scale structures computed directly. The resulting Reynolds-averaged Navier–Stokes equations for incompressible flow in a 2D vertical plane may be written in conservative form

$$\frac{\partial u}{\partial x}+\frac{\partial w}{\partial z}=0, \tag{1}$$

$$\frac{\partial u}{\partial t}+\frac{\partial (uu)}{\partial x}+\frac{\partial (wu)}{\partial z}=-\frac{1}{\rho}\frac{\partial p}{\partial x}+\frac{\partial}{\partial x}\left(v_{\mathrm{e}}\frac{\partial u}{\partial x}\right)+\frac{\partial}{\partial z}\left(v_{\mathrm{e}}\frac{\partial u}{\partial z}\right), \tag{2}$$

$$\frac{\partial w}{\partial t}+\frac{\partial (uw)}{\partial x}+\frac{\partial (ww)}{\partial z}=-g-\frac{1}{\rho}\frac{\partial p}{\partial x}+\frac{\partial}{\partial x}\left(v_{\mathrm{e}}\frac{\partial w}{\partial x}\right)+\frac{\partial}{\partial z}\left(v_{\mathrm{e}}\frac{\partial w}{\partial z}\right), \tag{3}$$

where x and z are the Cartesian co-ordinates in the horizontal and vertical directions (Figure 1), u and w are the velocity components in the x- and z-direction, g is the gravitational acceleration, p is the pressure, ρ is the fluid density. v_{e} is the eddy viscosity defined by the k–ϵ turbulence model [7]:

$$v_{\mathrm{e}}=v+c_{\mu}\frac{k^2}{\epsilon}, \tag{4}$$

in which v is kinematic viscosity, k is turbulence energy and ϵ is its dissipation rate.

k and ϵ are described by the standard transport equations [7] given in two dimensions as

$$\frac{\partial k}{\partial t}+\frac{\partial (uk)}{\partial x}+\frac{\partial (wk)}{\partial z}=\frac{\partial}{\partial x}\left(\frac{v_{\mathrm{e}}}{\sigma_k}\frac{\partial k}{\partial x}\right)+\frac{\partial}{\partial z}\left(\frac{v_{\mathrm{e}}}{\sigma_k}\frac{\partial k}{\partial z}\right)+P-\epsilon, \tag{5}$$

$$\frac{\partial \epsilon}{\partial t}+\frac{\partial (u\epsilon)}{\partial x}+\frac{\partial (w\epsilon)}{\partial z}=\frac{\partial}{\partial x}\left(\frac{v_{\mathrm{e}}}{\sigma_\epsilon}\frac{\partial \epsilon}{\partial x}\right)+\frac{\partial}{\partial z}\left(\frac{v_{\mathrm{e}}}{\sigma_\epsilon}\frac{\partial \epsilon}{\partial z}\right)+c_{1\epsilon}\frac{\epsilon}{\kappa}P-c_{2\epsilon}\frac{\epsilon^2}{k}, \tag{6}$$

where P is the turbulence production term and may be written in tensor notation,

$$P=v_{\mathrm{e}}\left(\frac{\partial u_i}{\partial x_j}+\frac{\partial u_j}{\partial x_i}\right)\frac{\partial u_i}{\partial x_j}, \tag{7}$$

where $i=1$, 2 corresponds to the x, z co-ordinates. The standard values of the turbulence constant are used: $c_{\mu}=0.09$, $c_{1\epsilon}=1.44$, $c_{2\epsilon}=1.92$, $\sigma_k=1.0$ and $\sigma_\epsilon=1.3$.

The linear pressure term p in Equations (2) and (3) can be split into two components, hydrostatic $\rho g(\eta-z)$ and non-hydrostatic $\tilde{p}$, giving

$$p=\rho g(\eta-z)+\tilde{p}, \tag{8}$$

where η is the water surface above horizontal datum (see Figure 1).

Substitution of Equation (8) into (2) and (3) leads to

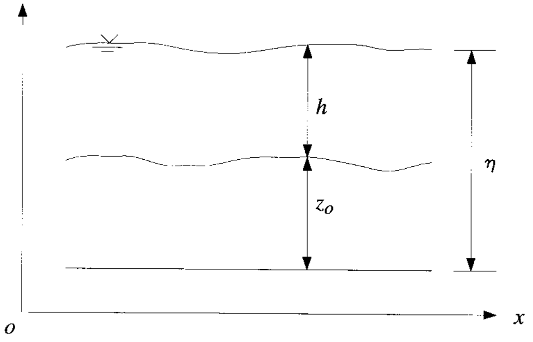

Figure 1. Definition sketch.

$$\frac{\partial u}{\partial t}+\frac{\partial(uu)}{\partial x}+\frac{\partial(wu)}{\partial z}=-g\frac{\partial\eta}{\partial x}-\frac{1}{\rho}\frac{\partial\tilde{p}}{\partial x}+\frac{\partial}{\partial x}\left(\nu_{\mathrm{e}}\frac{\partial u}{\partial x}\right)+\frac{\partial}{\partial z}\left(\nu_{\mathrm{e}}\frac{\partial u}{\partial z}\right), \tag{9}$$

$$\frac{\partial w}{\partial t}+\frac{\partial(uw)}{\partial x}+\frac{\partial(ww)}{\partial z}=-\frac{1}{\rho}\frac{\partial\tilde{p}}{\partial z}+\frac{\partial}{\partial x}\left(\nu_{\mathrm{e}}\frac{\partial w}{\partial x}\right)+\frac{\partial}{\partial z}\left(\nu_{\mathrm{e}}\frac{\partial w}{\partial z}\right). \tag{10}$$

By applying the kinematic condition at the free surface, the continuity equation (1) may be integrated over the depth to give the following free-surface equation

$$\frac{\partial\eta}{\partial t}+\frac{\partial}{\partial x}\int_{z_0}^{\eta}u\,\mathrm{d}z=0, \tag{11}$$

where z_0 is bed elevation above datum.

The σ-co-ordinate system for the vertical direction is used. It automatically fits the bed and free surface, enabling a mesh with high resolution to be produced in those regions. A Cartesian mesh inevitably has a ‘staircase’ structure at the bed and free surface giving poor resolution.

The σ-co-ordinate is defined as

$$\sigma=\frac{z-\eta}{h}. \tag{12}$$

In this co-ordinate system, velocities $u_\sigma=u$ and $w_\sigma=\omega/h$ (defined below), and Equations (9) and (10) may be written as

$$\frac{\partial(hu)}{\partial t}+\frac{\partial(huu)}{\partial x}+\frac{\partial(\omega u)}{\partial\sigma}=-gh\frac{\partial\eta}{\partial x}-\frac{h}{\rho}\frac{\partial\tilde{p}}{\partial x}+h\frac{\partial}{\partial x}\left(\nu_{\mathrm{e}}\frac{\partial u}{\partial x}\right)+\frac{\partial}{\partial\sigma}\left(\frac{\nu_{\mathrm{e}}}{h}\frac{\partial u}{\partial\sigma}\right), \tag{13}$$

$$\frac{\partial(hw)}{\partial t}+\frac{\partial(huw)}{\partial x}+\frac{\partial(\omega w)}{\partial\sigma}=-\frac{1}{\rho}\frac{\partial\tilde{p}}{\partial\sigma}+h\frac{\partial}{\partial x}\left(\nu_{\mathrm{e}}\frac{\partial w}{\partial x}\right)+\frac{\partial}{\partial\sigma}\left(\frac{\nu_{\mathrm{e}}}{h}\frac{\partial w}{\partial\sigma}\right), \tag{14}$$

where

$$\omega=w-u\left(\sigma\frac{\partial h}{\partial x}+\frac{\partial\eta}{\partial x}\right)-\left(\sigma\frac{\partial h}{\partial t}+\frac{\partial\eta}{\partial t}\right), \tag{15}$$

$\omega=0$ when $\sigma=-1$ or 0, corresponding to the bed and the free surface.

It should be explained why the horizontal gradient of non-hydrostatic pressure $\tilde{p}$ and the horizontal diffusion in Equations (13) and (14) are not transformed into the σ-co-ordinate system. These terms are calculated in the Cartesian frame to avoid large errors, particularly near a steep bed, resulting from the summation of large terms of opposite sign in the σ-co-ordinate transformation. The resulting truncation errors could cause spurious flows, particularly near the bed [8].

Similarly, Equations (5) and (6) can also be written in σ-co-ordinates, except for the horizontal diffusion terms, as

$$\frac{\partial(hk)}{\partial t}+\frac{\partial(huk)}{\partial x}+\frac{\partial(\omega k)}{\partial\sigma}=h\frac{\partial}{\partial x}\left(\frac{\nu_{\mathrm{e}}}{\sigma_k}\frac{\partial k}{\partial x}\right)+\frac{\partial}{\partial\sigma}\left(\frac{\nu_{\mathrm{e}}}{h\sigma_k}\frac{\partial k}{\partial\sigma}\right)+hP-h\epsilon, \tag{16}$$

$$\frac{\partial(h\epsilon)}{\partial t}+\frac{\partial(hu\epsilon)}{\partial x}+\frac{\partial(\omega\epsilon)}{\partial\sigma}=h\frac{\partial}{\partial x}\left(\frac{\nu_{\mathrm{e}}}{\sigma_\epsilon}\frac{\partial\epsilon}{\partial x}\right)+\frac{\partial}{\partial\sigma}\left(\frac{\nu_{\mathrm{e}}}{h\sigma_\epsilon}\frac{\partial\epsilon}{\partial\sigma}\right)+hc_{1\epsilon}\frac{\epsilon}{k}P-hc_{2\epsilon}\frac{\epsilon^2}{k}. \tag{17}$$

Equations (1), (11), (13), (14), (16) and (17) thus form the mathematical model for shallow-water flow with non-hydrostatic pressure.

In the present study, accurate resolution at both the bed and free surface is obtained using a non-uniform mesh. Namely, the parabolic transformation is used

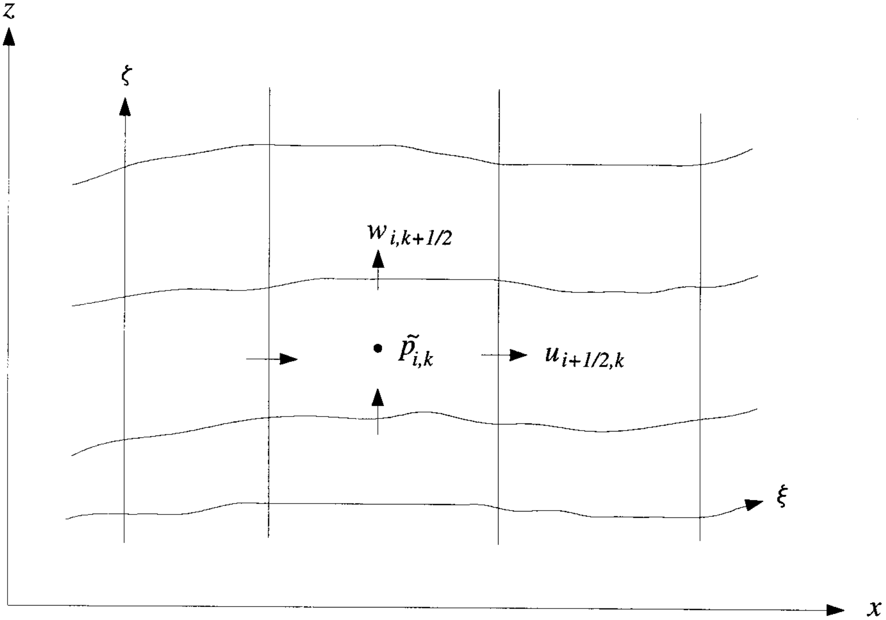

Figure 2. Staggered grid system showing velocity and pressure location in a cell.

$$\frac{\mathrm{d}\sigma_{\mathrm{mesh}}}{\mathrm{d}\sigma'_{\mathrm{mesh}}} = b(\sigma_{\mathrm{mesh}} + a)(1 - \sigma_{\mathrm{mesh}} + a) \tag{18}$$

to compress the σ mesh near the bed and surface symmetrically about the middepth, where $0 \leq \sigma_{\mathrm{mesh}} \leq 1$ defines the σ mesh and $0 \leq \sigma'_{\mathrm{mesh}} \leq 1$ is a uniformly spaced mesh. Clearly, $\sigma = \sigma_{\mathrm{mesh}} - 1$. The constant $a \ll 1$, and smaller values of a give a finer mesh near the bed and surface. b is calculated by

$$b = \frac{2}{1 + 2a} \log_{\mathrm{e}}(1 + 1/a). \tag{19}$$

3. DISCRETISED EQUATIONS AND SOLUTION METHOD

The staggered grid system shown in Figure 2 is used and the semi-implicit finite volume method follows that of Stansby [1]. To advance $\phi = u$, w, k and ϵ in Equations (13) and (14), we now write

$$h\frac{\partial \phi}{\partial t} = \frac{\partial (h\phi)}{\partial t} - \phi \frac{\partial h}{\partial t}. \tag{20}$$

The $\phi\, \partial h/\partial t$ item was not included in Stansby [1] and is very small for many shallow-water problems, but is included explicitly here for completeness. First-order time stepping is used because a very small time step is required for stability with k–ϵ turbulence modelling and there is little advantage in second-order (Crank–Nicolson) time stepping, at least for many problems, although this is available. The momentum equations take the following discretised form

$$u^{n+1}_{i+1/2,k} = Fu^{n}_{i+1/2,k} - g\frac{\delta t}{\delta x}(\eta^{n+1}_{i+1} - \eta^{n+1}_{i})$$
$$+\,\delta t\,\frac{(v^{n}_{\mathrm{e}}(\partial\sigma'/\partial\sigma))_{i+1/2,k+1/2}(u^{n+1}_{i+1/2,k+1} - u^{n+1}_{i+1/2,k}) - (v^{n}_{\mathrm{e}}(\partial\sigma'/\partial\sigma))_{i+1/2,k-1/2}(u^{n+1}_{i+1/2,k} - u^{n+1}_{i+1/2,k-1})}{(h^{n}_{i+1/2}\,\delta\sigma')^{2}(\partial\sigma/\partial\sigma')_{k}}, \tag{21}$$

$$w^{n+1}_{i,k+1/2} = Fw^{n}_{i,k+1/2}$$
$$+\,\delta t\,\frac{(v^{n}_{\mathrm{e}}(\partial\sigma'/\partial\sigma))_{i,k+1}(w^{n+1}_{i,k+3/2} - w^{n+1}_{i,k+1/2}) - (v^{n}_{\mathrm{e}}(\partial\sigma'/\partial\sigma))_{i,k}(w^{n+1}_{i,k+1/2} - w^{n+1}_{i,k-1/2})}{(h^{n}_{i}\,\delta\sigma')^{2}(\partial\sigma/\partial\sigma')_{k+1/2}}, \tag{22}$$

where n denotes the time level, δt is the time step and $\delta\sigma'$ is the vertical mesh spacing. There are additional terms associated with the bed and surface cells which are described later. Equations (21) and (22) can be written in matrix form

$$A^{n}_{i+1/2}U^{n+1}_{i+1/2} = G^{n}_{i+1/2} - g\frac{\delta t}{\delta x}(\eta^{n+1}_{i+1} - \eta^{n+1}_{i})h^{n}_{i+1/2}\Delta\sigma, \tag{23}$$

$$A^{n}_{i}W^{n+1}_{i} = G^{n}_{i}, \tag{24}$$

where

$$U^{n}_{i+1/2} = [u^{n}_{i+1/2,1}, u^{n}_{i+1/2,2}, \ldots, u^{n}_{i+1/2,K}]^{T}, \tag{25}$$

$$W^{n}_{i} = [w^{n}_{i+1/2}, w^{n}_{i,3/2}, \ldots, w^{n}_{i,K+1/2}]^{T}, \tag{26}$$

$$G^{n}_{i+1/2} = h^{n}_{i+1/2}\Delta\sigma^{T}[Fu^{n}_{i+1/2,1}, \ldots, Fu^{n}_{i+1/2,K}]^{T}, \tag{27}$$

$$G^{n}_{i} = h^{n}_{i}\Delta\sigma^{T}[Fw^{n}_{i,1/2}, \ldots, Fw^{n}_{i,K+1/2}]^{T}, \tag{28}$$

$$\Delta\sigma = [\delta\sigma_{1}, \delta\sigma_{2}, \ldots, \delta\sigma_{K}]^{T}, \tag{29}$$

$$\delta\sigma_{k} = \delta\sigma_{k+1/2} - \delta\sigma_{k-1/2}, \tag{30}$$

and A will be defined later with terms defining the bed and free-surface conditions and new terms resulting from the bed slope not being small.

The free-surface equation (11) can be discretised and written in the following matrix notation

$$\eta^{n+1}_{i} = \eta^{n}_{i} - \frac{\delta t}{\delta x}(h^{n}_{i+1/2}\Delta\sigma^{T}U^{n+1}_{i+1/2} - h^{n}_{i-1/2}\Delta\sigma^{T}U^{n+1}_{i-1/2}). \tag{31}$$

Substitution of U from Equation (23) into this equation yields

$$\eta^{n+1}_{i} - g\left(\frac{\delta t}{\delta x}\right)^{2}[(h^{n}_{i+1/2})^{2}\Delta\sigma^{T}A^{-1}_{i+1/2}\Delta\sigma(\eta^{n+1}_{i+1} - \eta^{n+1}_{i})$$
$$- (h^{n}_{i-1/2})^{2}\Delta\sigma^{T}A^{-1}_{i-1/2}\Delta\sigma(\eta^{n+1}_{i} - n^{n+1}_{i-1})]$$
$$= \eta^{n}_{i} - \frac{\delta t}{\delta x}[h^{n}_{i+1/2}(\Delta\sigma^{T}A^{-1}_{i+1/2}G_{i+1/2})^{n} - h^{n}_{i-1/2}(\Delta\sigma^{T}A^{-1}_{i-1/2}G_{i-1/2})^{n}]. \tag{32}$$

The explicit operator $F\phi$ includes advection $F\phi^{a}$, horizontal diffusion $F\phi^{d}$, non-hydrostatic pressure gradient $F\phi^{p}$ and the $\phi\,\partial h/\partial t$ term $F\phi^{h}$, where ϕ stands for u in Equation (21) and w in Equation (22). $F\phi^{a}$ is given by (using the notation in Figure 3)

$$F\phi^a_{\mathrm{P}} = -\frac{\delta t}{h}\left(\frac{u_{\mathrm{e}}(h\phi)_{\mathrm{e}} - u_{\mathrm{w}}(h\phi)_{\mathrm{w}}}{\delta x} + \frac{\omega_{\mathrm{u}}\phi_{\mathrm{u}} - \omega_{\mathrm{d}}\phi_{\mathrm{d}}}{\delta\sigma'(\partial\sigma/\partial\sigma')}\right), \tag{33}$$

where terms u_{e}, u_{w}, ω_{u}, ω_{d} are obtained by linear interpolation, also h is determined by linear interpolation where necessary. The linear upwind difference scheme (LUDS) is used to express the variables at the cell faces, e, w and u, d, giving

$$(h\phi)_{\mathrm{e}} = \begin{cases} (3(h\phi)_{\mathrm{P}} - (h\phi)_{\mathrm{W}})/2 & \text{if } u_{\mathrm{e}} > 0, \\ (3(h\phi_{\mathrm{E}}) - (h\phi)_{\mathrm{EE}})/2 & \text{if } u_{\mathrm{e}} \le 0, \end{cases} \tag{34}$$

$$\phi_{\mathrm{u}} = \begin{cases} (3\phi_{\mathrm{P}} - \phi_{\mathrm{D}})/2 & \text{if } \omega_{\mathrm{u}} > 0, \\ (e\phi_{\mathrm{U}} - \phi_{\mathrm{UU}})/2 & \text{if } \omega_{\mathrm{u}} \le 0. \end{cases} \tag{35}$$

The horizontal diffusion term Fu^d may be approximated in real space by a finite volume approach,

$$\begin{aligned} Fu^d_{i+1/2,k} = {} & \frac{\delta t}{h_{i+1/2}\delta x}\left(\nu_{\mathrm{e}}\frac{\partial u}{\partial x}_{i+1,k} h_{i+1} - \nu_{\mathrm{e}}\frac{\partial u}{\partial x}_{i,k} h_i\right) \\ & - \frac{\delta t(h_{i+1} - h_i)\delta\sigma_{k+1/2}}{2h_{i+1/2}\,\delta\sigma_k\,\delta x}\left(\nu_{\mathrm{e}}\frac{\partial u}{\partial x}_{i+1,k+1/2} + \nu_{\mathrm{e}}\frac{\partial u}{\partial x}_{i,k+1/2}\right) \\ & + \frac{\delta t(h_{i+1} - h_i)\delta\sigma_{k-1/2}}{2h_{i+1/2}\,\delta\sigma_k\,\delta x}\left(\nu_{\mathrm{e}}\frac{\partial u}{\partial x}_{i+1,k-1/2} + \nu_{\mathrm{e}}\frac{\partial u}{\partial x}_{i,k-1/2}\right), \end{aligned} \tag{36}$$

with a corresponding formulation for Fw^d. There are now additional terms at the bed, because the slope is not necessarily small. These are defined later.

The non-hydrostatic pressure gradient terms, $F\phi^p$, in Equation (21) for u and (22) for w, are respectively,

$$Fu^p = -\frac{\delta t}{\rho}\frac{\partial\tilde{p}}{\partial x}, \qquad Fw^p = -\frac{\delta t}{h\rho}\frac{\partial\tilde{p}}{\partial\sigma}, \tag{37}$$

and

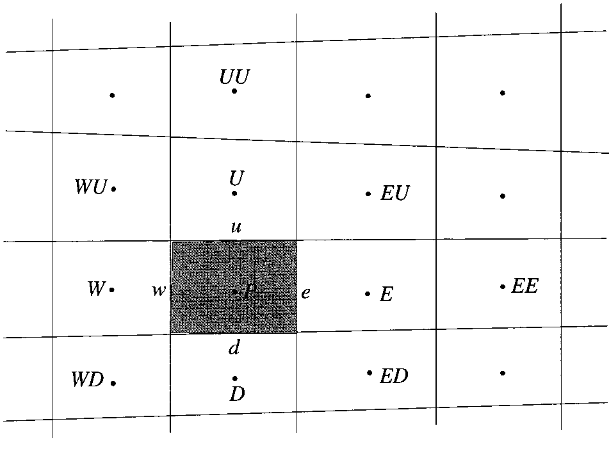

Figure 3. Control volume and cell face notation (Note U, D for up and down is used in vertical equivalent to N, S for north and south used for 3D problems).

$$F\phi^h = -\frac{\phi^n}{h^n}(h^n - h^{n-1}). \tag{38}$$

The complete expressions for Fu and Fw are $Fu = u + Fu^a + Fu^d + Fu^p + Fu^h$ and $Fw = w + Fw^a + Fw^d + Fw^p + Fw^h$.

Equation (32) is solved to give η and Equations (23) and (24) are then solved for u and w. k and ϵ are then advanced in time with a discretisation of Equations (16) and (17) as in Reference [1].

The computed velocities will not accurately satisfy the local continuity equation and the non-hydrostatic pressure $\tilde{p}$ must be corrected to achieve this. The velocities may be then modified accordingly. If the correction for the non-hydrostatic pressure is p', the corrected value is given by

$$\tilde{p} = \tilde{p}^* + p', \tag{39}$$

where * denotes the uncorrected value.

The new velocities which satisfy continuity can be derived from the discretised momentum equations (21) and (22), as

$$u = u^* - \frac{\delta t}{\rho}\frac{\partial p'}{\partial x}, \tag{40}$$

$$w = w^* - \frac{\delta t}{\rho}\frac{\partial p'}{\partial z}. \tag{41}$$

In deriving an equation set for the solution of p', the σ-co-ordinate system is equivalent to a conventional curvilinear co-ordinate system and this derivation will be pursued here. Curvilinear co-ordinates $\xi = \xi(x, z)$ and $\zeta = \zeta(x, z)$ are thus introduced. Accordingly, partial derivatives of a function φ are transformed to

$$\varphi_x = \frac{(z_\zeta \varphi_\xi - z_\xi \varphi_\zeta)}{J}, \qquad \varphi_z = \frac{(-x_\zeta \varphi_\xi + x_\xi \varphi_\zeta)}{J}, \tag{42}$$

where $J = x_\xi z_\zeta - x_\zeta z_\xi$ is the Jacobian of the transformation.

Equations (40) and (41) can be written in curvilinear co-ordinates as

$$u = u^* - \frac{\delta t}{\rho}\frac{(z_\zeta p'_\xi - z_\xi p'_\zeta)}{J}, \tag{43}$$

$$w = w^* - \frac{\delta t}{\rho}\frac{(-x_\zeta p'_\xi + x_\xi p'_\zeta)}{J}. \tag{44}$$

The continuity equation (1) becomes

$$\frac{(z_\zeta u_\xi - z_\xi u_\zeta)}{J} + \frac{(-x_\zeta w_\xi + x_\xi w_\zeta)}{J} = 0, \tag{45}$$

or

$$(z_\zeta u_\xi - x_\zeta w_\xi) + (x_\xi w_\zeta - z_\xi u_\zeta) = 0. \tag{46}$$

Integrating Equation (46) over the control volume shown in Figure 3 gives

$$\delta\zeta[(z_\zeta u - x_\zeta w)_{\mathrm{e}} - (z_\zeta u - x_\zeta w)_{\mathrm{w}}] + \delta\xi[(x_\xi w - z_\xi u)_{\mathrm{u}} - (x_\xi w - z_\xi u)_{\mathrm{d}}] = 0. \tag{47}$$

Substitution of Equations (43) and (44) into (47) results in the following pressure correction equation, which includes all eight neighbouring points around grid point P under consideration.

$$a_{\mathrm{P}}p'_{\mathrm{P}} = a_{\mathrm{E}}p'_{\mathrm{E}} + a_{\mathrm{W}}p'_{\mathrm{W}} + a_{\mathrm{U}}p'_{\mathrm{U}} + a_{\mathrm{D}}p'_{\mathrm{D}} + a_{\mathrm{EU}}p'_{\mathrm{EU}} + a_{\mathrm{ED}}p'_{\mathrm{ED}} + a_{\mathrm{WU}}p'_{\mathrm{WU}} + a_{\mathrm{WD}}p'_{\mathrm{WD}} + a_0, \tag{48}$$

where

$$a_{\mathrm{E}} = \left(\frac{x_\zeta^2 + z_\zeta^2}{J}\,\delta\zeta\right)_{\mathrm{e}} - \left(\frac{x_\xi x_\zeta + z_\xi z_\zeta}{4J}\,\delta\xi\right)_{\mathrm{u}} + \left(\frac{x_\xi x_\zeta + z_\xi z_\zeta}{4J}\,\delta\xi\right)_{\mathrm{d}}, \tag{49}$$

$$a_{\mathrm{W}} = \left(\frac{x_\zeta^2 + z_\zeta^2}{J}\,\delta\zeta\right)_{\mathrm{w}} + \left(\frac{x_\xi x_\zeta + z_\xi z_\zeta}{4J}\,\delta\xi\right)_{\mathrm{u}} - \left(\frac{x_\xi x_\zeta + z_\xi z_\zeta}{4J}\,\delta\xi\right)_{\mathrm{d}}, \tag{50}$$

$$a_{\mathrm{U}} = \left(\frac{x_\xi^2 + z_\xi^2}{J}\,\delta\zeta\right)_{\mathrm{u}} - \left(\frac{x_\xi x_\zeta + z_\xi z_\zeta}{4J}\,\delta\zeta\right)_{\mathrm{e}} + \left(\frac{x_\xi x_\zeta + z_\xi z_\zeta}{4J}\,\delta\zeta\right)_{\mathrm{w}}, \tag{51}$$

$$a_{\mathrm{D}} = \left(\frac{x_\xi^2 + z_\xi^2}{J}\,\delta\xi\right)_{\mathrm{d}} + \left(\frac{x_\xi x_\zeta + z_\xi z_\zeta}{4J}\,\delta\zeta\right)_{\mathrm{e}} - \left(\frac{x_\xi x_\zeta + z_\xi z_\zeta}{4J}\,\delta\zeta\right)_{\mathrm{w}}, \tag{52}$$

$$a_{\mathrm{EU}} = -\left(\frac{x_\xi x_\zeta + z_\xi z_\zeta}{4J}\,\delta\zeta\right)_{\mathrm{e}} - \left(\frac{x_\xi x_\zeta + z_\xi z_\zeta}{4J}\,\delta\xi\right)_{\mathrm{u}}, \tag{53}$$

$$a_{\mathrm{ED}} = \left(\frac{x_\xi x_\zeta + z_\xi z_\zeta}{4J}\,\delta\zeta\right)_{\mathrm{e}} + \left(\frac{x_\xi x_\zeta + z_\xi z_\zeta}{4J}\,\delta\xi\right)_{\mathrm{d}}, \tag{54}$$

$$a_{\mathrm{WU}} = \left(\frac{x_\xi x_\zeta + z_\xi z_\zeta}{4J}\,\delta\zeta\right)_{\mathrm{w}} + \left(\frac{x_\xi x_\zeta + z_\xi z_\zeta}{4J}\,\delta\xi\right)_{\mathrm{u}}, \tag{55}$$

$$a_{\mathrm{WD}} = -\left(\frac{x_\xi x_\zeta + z_\xi z_\zeta}{4J}\,\delta\zeta\right)_{\mathrm{w}} - \left(\frac{x_\xi x_\zeta + z_\xi z_\zeta}{4J}\,\delta\xi\right)_{\mathrm{d}}, \tag{56}$$

$$a_{\mathrm{P}} = \left(\frac{x_\zeta^2 + z_\zeta^2}{J}\,\delta\zeta\right)_{\mathrm{e}} + \left(\frac{x_\zeta^2 + z_\zeta^2}{J}\,\delta\zeta\right)_{\mathrm{w}} + \left(\frac{x_\xi^2 + z_\xi^2}{J}\,\delta\xi\right)_{\mathrm{u}} + \left(\frac{x_\xi^2 + z_\xi^2}{J}\,\delta\xi\right)_{\mathrm{d}}, \tag{57}$$

and

$$a_0 = \frac{\rho}{\delta t}\,\{\delta\zeta[(z_\zeta u^* - x_\zeta w^*)_{\mathrm{w}} - (z_\zeta u^* - x_\zeta w^*)_{\mathrm{e}}] + \delta\xi[(x_\xi w^* - z_\xi u^*)_{\mathrm{d}} - (x_\xi w^* - z_\xi u^*)_{\mathrm{u}}]\}. \tag{58}$$

In the present study, the conjugate gradient method is used to solve the pressure correction equation (48). The non-hydrostatic pressure and velocities are then updated through Equations (39), (43) and (44).

The whole solution procedure for a time step is now summarised below:

1. initial values for u, w, η, k, ϵ and $\tilde{p}$ are known
2. compute v_{e} from Equation (4)
3. solve the free-surface equation (32) to obtain η
4. solve momentum equations (21) and (22) to obtain u^* and w^*
5. solve Equation (48) to obtain the correction p' for non-hydrostatic pressure
6. update the non-hydrostatic pressure and velocities from Equations (39), (43) and (44)
7. solve the k-equation (16)
8. solve the ϵ-equation (17)

4. BOUNDARY CONDITIONS

The cells at the bed and free surface require special treatment. At the bed, with the hydrostatic pressure assumption the effect of horizontal diffusion may be assumed to be small in relation to vertical diffusion. However, this is not necessarily the case with non-hydrostatic pressure where the bed slope is not small and a more general formulation needs to be derived. Standard wall functions are used within the wall region ($30 < D_{\mathrm{n}} V_{*}/\nu < 100$), where D_{n} is the normal distance from the bed, and a bed cell should lie within this region. The normal pressure gradient at the bed is set to zero, the standard boundary-layer assumption. The velocity parallel to the bed is described by the logarithmic law,

$$\frac{V_\tau}{V_*} = \frac{1}{\kappa} \log_{\mathrm{e}} C, \tag{59}$$

where V_τ is velocity parallel to the wall and

$$C = \begin{cases} \dfrac{30.0}{k_s} D_{\mathrm{n}} & \text{Rough bed of equivalent roughness height } k_s, \\ \dfrac{9.05 V_* D_{\mathrm{n}}}{\nu} & \text{Smooth bed.} \end{cases} \tag{60}$$

The shear velocity is thus defined by

$$V_* = \frac{V_\tau}{(1/\kappa) \log_{\mathrm{e}} C}. \tag{61}$$

Consequently, the shear stress at the wall is calculated as

$$\tau_{\mathrm{w}} = \rho V_*^2 = \frac{\rho V_\tau^2}{((1/\kappa) \log_{\mathrm{e}} C)^2}, \tag{62}$$

which can also be written in general vector form (for two- or three-dimensional situations)

$$\vec{\tau}_{\mathrm{w}} = -\frac{\rho |\vec{V}_\tau^2|}{((1/\kappa) \log_{\mathrm{e}} C)^2} \vec{V}_\tau. \tag{63}$$

To determine the bed conditions with a finite volume formulation, it is convenient to write the momentum equations (2) and (3) in vector form as

$$\frac{\partial \vec{V}}{\partial t} + \nabla \cdot (\vec{V}\vec{V}) = \mathbf{f} - \frac{1}{\rho} \nabla p + \nabla \cdot (\nu_{\mathrm{e}} \nabla \vec{V}), \tag{64}$$

where $\mathbf{f} = -g\vec{k}$ is the gravity force and $\vec{V} = u\vec{i} + w\vec{k}$ is the velocity vector.

Integrating over the area $\overline{abcd}$ for grid point P, shown in Figure 4, gives

$$\iint \frac{\partial \vec{V}}{\partial t} \, \mathrm{d}\Omega + \iint \nabla \cdot (\vec{V}\vec{V}) \, \mathrm{d}\Omega = \iint \mathbf{f} \, \mathrm{d}\Omega - \iint \frac{1}{\rho} \nabla p \, \mathrm{d}\Omega + \iint \nabla \cdot (\nu_{\mathrm{e}} \nabla \vec{V}) \, \mathrm{d}\Omega, \tag{65}$$

where Ω is area. The advection term in Equation (65) can be evaluated in the manner already described. The pressure gradient terms are defined by the tangential and normal values. The diffusion term, however, needs special attention.

Applying the Gauss divergence theorem gives

$$\iint \nabla \cdot (\nu_{\mathrm{e}} \nabla \vec{V}) \, \mathrm{d}\Omega = \oint_S \vec{n}_s \cdot (\nu_{\mathrm{e}} \nabla \vec{V}) \, \mathrm{d}S, \tag{66}$$

where S is the length around the cell boundary and $\vec{n}_s$ is the outward unit vector normal to the cell face.

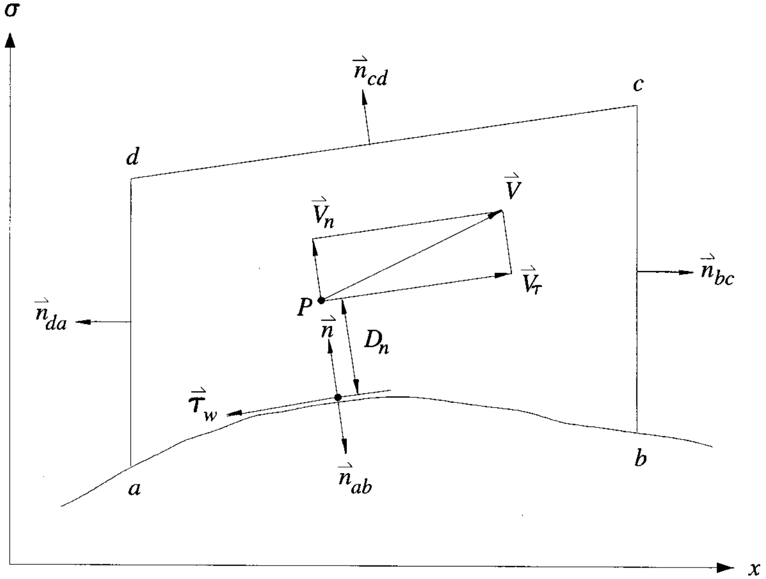

Figure 4. Control volume close to wall.

The right-hand-side of Equation (66) can be expanded as

$$\underbrace{\int_{S_{ab}} \vec{n}_{ab}\cdot(\nu_{\rm e}\nabla\vec{V})\,{\rm d}S}_{\rm (I)} + \underbrace{\int_{S_{bc}} \vec{n}_{bc}\cdot(\nu_{\rm e}\nabla\vec{V})\,{\rm d}S}_{\rm (II)} + \underbrace{\int_{S_{cd}} \vec{n}_{cd}\cdot(\nu_{\rm e}\nabla\vec{V})\,{\rm d}S}_{\rm (III)} + \underbrace{\int_{S_{da}} \vec{n}_{da}\cdot(\nu_{\rm e}\nabla\vec{V})\,{\rm d}S}_{\rm (IV)}, \tag{67}$$

where the unit vectors at the cell faces $\overline{ab}$, $\overline{cd}$, $\overline{bc}$ and $\overline{da}$ can be expressed in Cartesian terms

$$\vec{n}_{ab} = n_{abx}\vec{i} + n_{abz}\vec{k}, \qquad \vec{n}_{cd} = n_{cdx}\vec{i} + n_{cdz}\vec{k}, \tag{68}$$

and

$$\vec{n}_{bc} = \vec{i}, \qquad \vec{n}_{da} = -\vec{i}. \tag{69}$$

Substituting Equation (69) into terms (II) and (IV) in Equation (67) gives

$$\mathrm{II} = \int_{S_{bc}} \vec{i}\cdot(\nu_{\rm e}\nabla\vec{V})\,{\rm d}S = \left(h\delta\sigma\nu_{\rm e}\frac{\partial\vec{V}}{\partial x}\right)_{\rm e}, \tag{70}$$

$$\mathrm{IV} = -\int_{S_{da}} \vec{i}\cdot(\nu_{\rm e}\nabla\vec{V})\,{\rm d}S = -\left(h\delta\sigma\nu_{\rm e}\frac{\partial\vec{V}}{\partial x}\right)_{\rm w}. \tag{71}$$

These two terms are equivalent to the first term on the right-hand-side of Equation (36), which defines the explicit horizontal diffusion terms for u-momentum.

Since $\vec{n}_{cd} = n_{cdx}\vec{i} + n_{cdz}\vec{k}$, term (III) can be written

$$\mathrm{III} = \int_{S_{cd}} (n_{cdx}\vec{i} + n_{cdz}\vec{k})\cdot(\nu_{\rm e}\nabla\vec{V})\,{\rm d}S = n_{cdx}S_{cd}\left(\nu_{\rm e}\frac{\partial\vec{V}}{\partial x}\right)_{\rm n} + n_{cdz}S_{cd}\left(\nu_{\rm e}\frac{\partial\vec{V}}{\partial z}\right)_{\rm n}. \tag{72}$$

The first term on the right-hand-side of Equation (72), is equivalent to the second term in Equation (36). The second term in Equation (72) with $n_{cdz}S_{cd} = \delta x$ is a vertical diffusion term, compatible with Equation (21), and is treated implicitly.

Term (I) requires the use of wall functions to define the velocity gradient at the wall boundary $\overline{ab}$. The velocity vector $\vec{V}$ may be decomposed into velocity vector $\vec{V}_\tau$ parallel to the wall and $\vec{V}_\mathrm{n}$ normal to the wall, i.e. $\vec{V} = \vec{V}_\tau + \vec{V}_\mathrm{n}$. Hence, term (I) may be written

$$\mathrm{I} = \int_{S_{ab}} \vec{n}_{ab} \cdot (\nu_\mathrm{e} \nabla \vec{V}_\tau)\, \mathrm{d}S + \int_{S_{ab}} \vec{n}_{ab} \cdot (\nu_\mathrm{e} \nabla \vec{V}_n)\, \mathrm{d}S. \tag{73}$$

Since $\vec{n}_{ab} = -\vec{n}$ (see Figure 4), Equation (73) can now be written

$$\mathrm{I} = -\int_{S_{ab}} \vec{n} \cdot (\nu_\mathrm{e} \nabla \vec{V}_\tau)\, \mathrm{d}S - \int_{S_{ab}} \vec{n} \cdot (\nu_\mathrm{e} \nabla \vec{V}_\mathrm{n})\, \mathrm{d}S, \tag{74}$$

and approximated as

$$\mathrm{I} = -S_{ab} \nu_\mathrm{e} \frac{\partial \vec{V}_\tau}{\partial n} - S_{ab} \nu_\mathrm{e} \frac{\partial \vec{V}_\mathrm{n}}{\partial n}. \tag{75}$$

It should be pointed out that the second term on the right-hand-side of Equation (75) has been neglected in shallow-water simulations with the assumption of hydrostatic pressure and small bed slope. However, if the bed slope is not small, it may have the same order of magnitude as the first term and should not be ignored. Its inclusion is consistent with incorporating non-hydrostatic pressure.

Obviously, $\vec{V}_\mathrm{n} = 0$ (note $\partial \vec{V}_\mathrm{n}/\partial n \neq 0$) at the bed and $\nu_\mathrm{e} \partial \vec{V}_\tau/\partial n = -\vec{\tau}_\mathrm{w}/\rho$ with $\vec{\tau}_\mathrm{w}$ defined by the wall function (63). Thus, Equation (75) can be written

$$\mathrm{I} = -S_{ab} \frac{|\vec{V}_\tau|_\mathrm{P}}{((1/\kappa)\log_\mathrm{e} C)^2} (\vec{V}_\tau)_\mathrm{P} - S_{ab} \nu_\mathrm{e} \frac{(\vec{V}_\mathrm{n})_\mathrm{P}}{D_\mathrm{n}}. \tag{76}$$

From vector analysis, $\vec{V}_\tau$ and $\vec{V}_\mathrm{n}$ may be defined as

$$\vec{V}_\tau = \vec{V} - (\vec{V} \cdot \vec{n})\vec{n} = [(1 - n_x^2)u - n_x n_z w]\vec{i} + [-n_x n_z u + (1 - n_z^2)w]\vec{k}, \tag{77}$$

$$\vec{V}_\mathrm{n} = (\vec{V} \cdot \vec{n})\vec{n} = [n_x^2 u + n_x n_z w]\vec{i} + [n_x n_z u + n_z^2 w]\vec{k}, \tag{78}$$

where n_x and n_z are the components of the unit vector $\vec{n}$ in the x- and z-directions.

Substitution of Equations (77) and (78) into (76) results in

$$\begin{aligned} \mathrm{I} = &-S_{ab}\left[\frac{|\vec{V}_\tau|_\mathrm{P}}{((1/\kappa)\log_\mathrm{e} C)^2}\,(1 - n_x^2) + \frac{\nu}{D_\mathrm{n}} n_x^2\right] u\vec{i} + S_{ab} n_x n_z \left[\frac{|\vec{V}_\tau|_\mathrm{P}}{((1/\kappa)\log_\mathrm{e} C)^2} - \frac{\nu}{D_\mathrm{n}}\right] w\vec{i} \\ &- S_{ab}\left[\frac{|\vec{V}_\tau|_\mathrm{P}}{((1/\kappa)\log_\mathrm{e} C)^2}(1 - n_x^2) + \frac{\nu}{D_\mathrm{n}} n_z^2\right] w\vec{k} + S_{ab} n_x n_z \left[\frac{|\vec{V}_\tau|_\mathrm{P}}{((1/\kappa)\log_\mathrm{e} C)^2} - \frac{\nu}{D_\mathrm{n}}\right] u\vec{k}. \end{aligned} \tag{79}$$

This gives the standard and new terms for the bed cells in the u- and w-momentum equations (20) and (21). The last term on the right-hand-side of Equation (36) is zero. The second and the last terms in Equation (79) are new and are treated explicitly in the u- and w-momentum equations (added to the F operator). The first and third terms are treated implicitly and included in the A matrix defined below; they approach the standard terms as bed slope decreases.

At the free surface, $\tilde{p} = 0$ and $\partial u/\partial z = 0$ without wind stress. w is determined in a surface cell by applying the continuity equation

$$\frac{\partial w}{\partial z} = -\frac{\partial u}{\partial x}. \tag{80}$$

The complete matrix $A_{i+1/2}^n$ in Equation (23) may now be specified

$$A^n_{i+1/2} = \left|\begin{array}{ccccccc} a_{11} & a_{12} & & & & & \\ a_{21} & a_{22} & a_{23} & & & & \\ & \cdots & \cdots & \cdots & & & \\ & & a_{k,k-1} & a_{k,k} & a_{k,k+1} & & \\ & & & \cdots & \cdots & \cdots & \\ & & & & a_{K,K-1} & a_{K,K} & \end{array}\right|,$$

where K is the number of cells in a vertical layer and

$$a_{11} = 1 + \frac{\delta t(\nu^n_{\mathrm{e}}(\partial\sigma'/\partial\sigma))_{i+1/2,1(1/2)}}{\delta\sigma'(h^n_{i+1/2})^2(\sigma_{1(1/2)}-\sigma_{1/2})} + \frac{\delta t S_{ab}}{\delta x h^n_{i+1/2}(\sigma_{1(1/2)}-\sigma_{1/2})}\left[\frac{|\vec{V}_\tau|_{\mathrm{P}}}{((1/\kappa)\log_{\mathrm{e}} C)^2}(1-n_x^2)+\frac{\nu}{D_{\mathrm{n}}}n_x^2\right], \tag{81}$$

$$a_{12} = -\frac{\delta t(\nu^n_{\mathrm{e}}(\partial\sigma'/\partial\sigma))_{i+1/2,1(1/2)}}{\delta\sigma'(h^n_{i+1/2})^2(\sigma_{1(1/2)}-\sigma_{1/2})}, \tag{82}$$

$$a_{k,k-1} = -\frac{\delta t(\nu^n_{\mathrm{e}}(\partial\sigma'/\partial\sigma))_{i+1/2,k-1/2}}{\delta\sigma'(h^n_{i+1/2})^2(\sigma_{k+1/2}-\sigma_{k-1/2})}, \tag{83}$$

$$a_{k,k} = 1 + \frac{\delta t(\nu^n_{\mathrm{e}}(\partial\sigma'/\partial\sigma))_{i+1/2,k-1/2}}{\delta\sigma'(h^n_{i+1/2})^2(\sigma_{k+1/2}-\sigma_{k-1/2})} + \frac{\delta t(\nu^n_{\mathrm{e}}(\partial\sigma'/\partial\sigma))_{i+1/2,k+1/2}}{\delta\sigma'(h^n_{i+1/2})^2(\sigma_{k+1/2}-\sigma_{k-1/2})}, \tag{84}$$

$$a_{k,k+1} = -\frac{\delta t(\nu^n_{\mathrm{e}}(\partial\sigma'/\partial\sigma))_{i+1/2,k+1/2}}{\delta\sigma'(h^n_{i+1/2})^2(\sigma_{k+1/2}-\sigma_{k-1/2})}, \tag{85}$$

$$a_{K,K-1} = -\frac{\delta t(\nu^n_{\mathrm{e}}(\partial\sigma'/\partial\sigma))_{i+1/2,K-1/2}}{\delta\sigma'(h^n_{i+1/2})^2(\sigma_{K+1/2}-\sigma_{K-1/2})}, \tag{86}$$

$$a_{K,K} = 1 + \frac{\delta t(\nu^n_{\mathrm{e}}(\partial\sigma'/\partial\sigma))_{i+1/2,K-1/2}}{\delta\sigma'(h^n_{i+1/2})^2(\sigma_{K+1/2}-\sigma_{K-1/2})}. \tag{87}$$

The numerical scheme for advancing k and ϵ is unchanged from the scheme with the hydrostatic pressure assumption [1] using standard bed and surface boundary conditions. Reynolds stress is assumed constant across the wall region and turbulence production equals its dissipation giving the boundary condition for k and ϵ

$$k = \frac{V_*^2}{\sqrt{c_\mu}}, \tag{88}$$

$$\epsilon = \frac{|V_*|^3}{\kappa D_{\mathrm{n}}}. \tag{89}$$

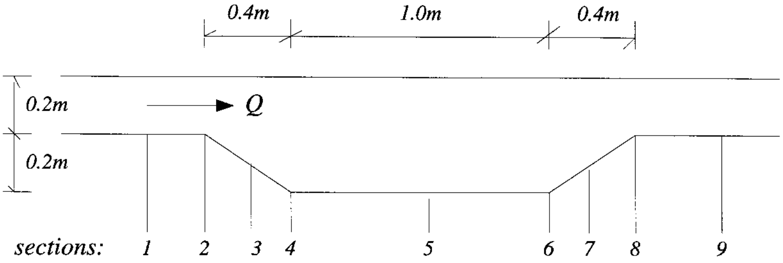

Figure 5. Trench layout and dimension.

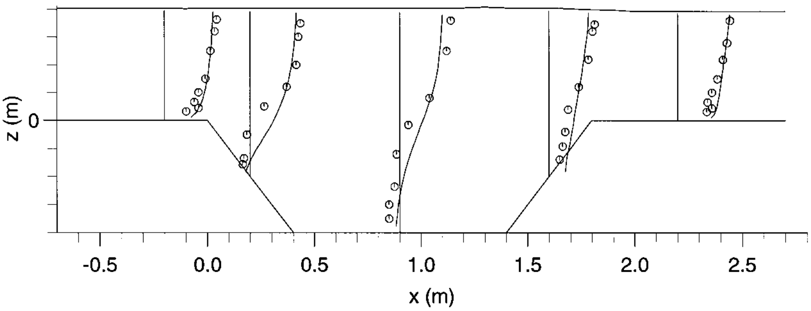

Figure 6. Comparison of mean velocity u- in x-direction with experimental results shown by circles.

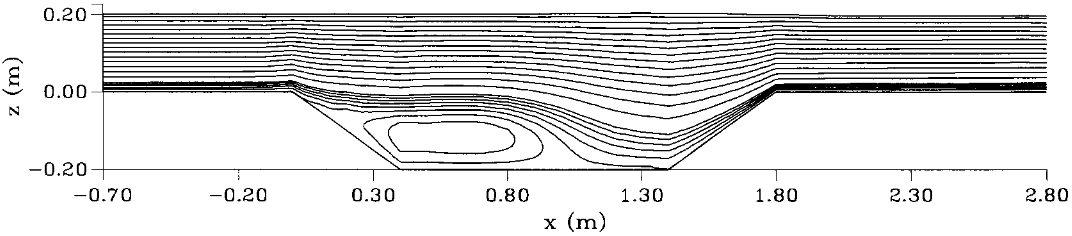

Figure 7. Streamlines in trench.

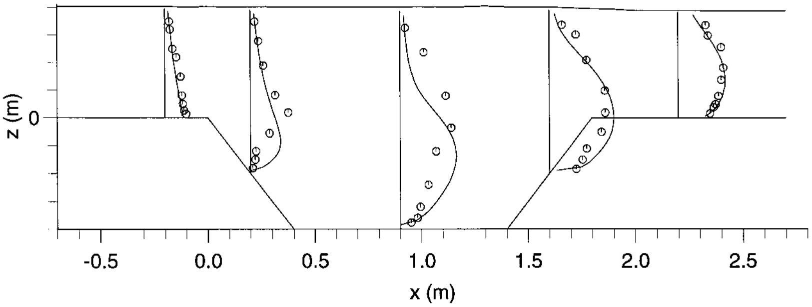

Figure 8. Comparison of turbulence energy k with experimental results shown by circles.

At the surface, k and ϵ are defined by

$$\frac{\partial k}{\partial z} = 0, \tag{90}$$

$$\epsilon = (k\sqrt{c_\mu})^{1.5}/(0.07\kappa h). \tag{91}$$

It remains to define the inflow and outflow boundary conditions.

4.1. Inflow boundary

At inflow, the velocity components and turbulence variables are specified using either the standard formulae for open channel flow,

$$\frac{u}{V_*} = \begin{cases} \dfrac{1}{\kappa}\log_e\left(\dfrac{30.0(z-z_0)}{k_s}\right) & \text{Rough bed,} \\ \dfrac{1}{\kappa}\log_e\left(\dfrac{9.05V_*(z-z_0)}{\nu}\right) & \text{Smooth bed,} \end{cases} \tag{92}$$

$$w = 0, \tag{93}$$

$$k = \frac{V_*^2}{c_\mu^{0.5}}\left(1 - \frac{z}{h}\right), \tag{94}$$

$$\epsilon = \frac{|V_*|^3}{\kappa z}\left(1 - \frac{z}{h}\right), \tag{95}$$

or more simply, homogeneous turbulence is sometimes specified as

$$u = \text{constant}, \tag{96}$$

$$w = 0, \tag{97}$$

$$k = 0.03u^2, \tag{98}$$

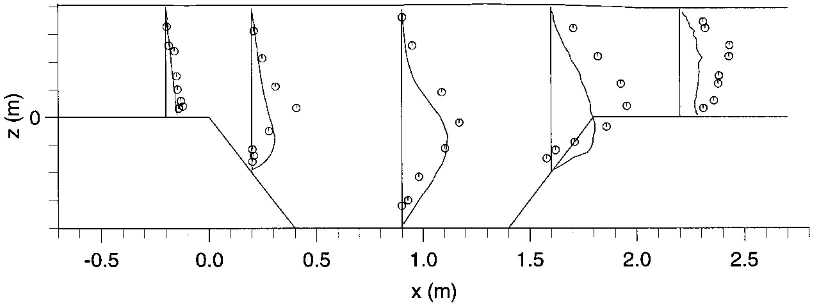

Figure 9. Comparison of shear stress τ_{xz} with experimental results shown by circles.

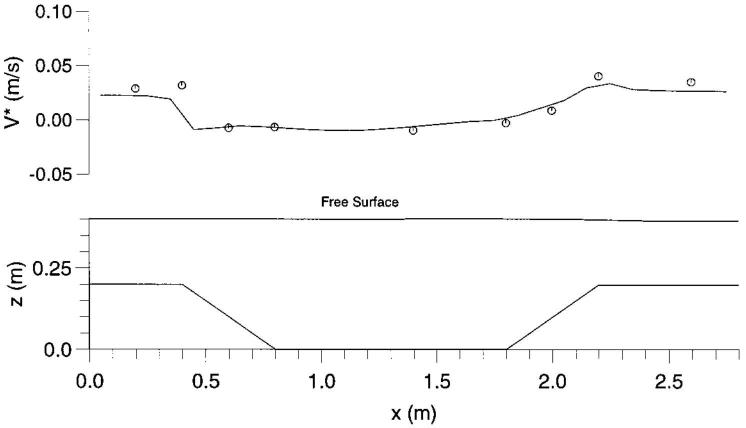

Figure 10. Comparison of friction velocity V_* with experimental results shown by circles.

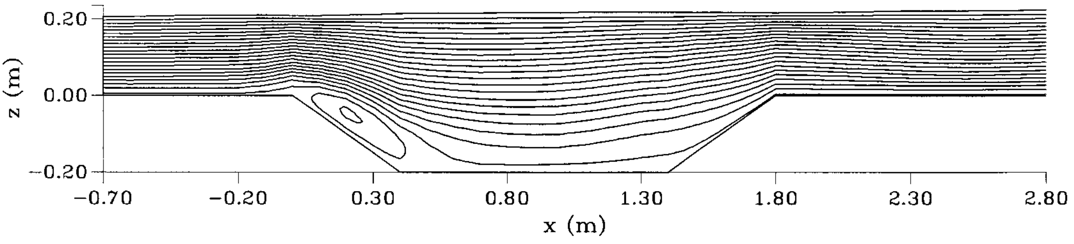

Figure 11. Streamlines of computation with hydrostatic pressure.

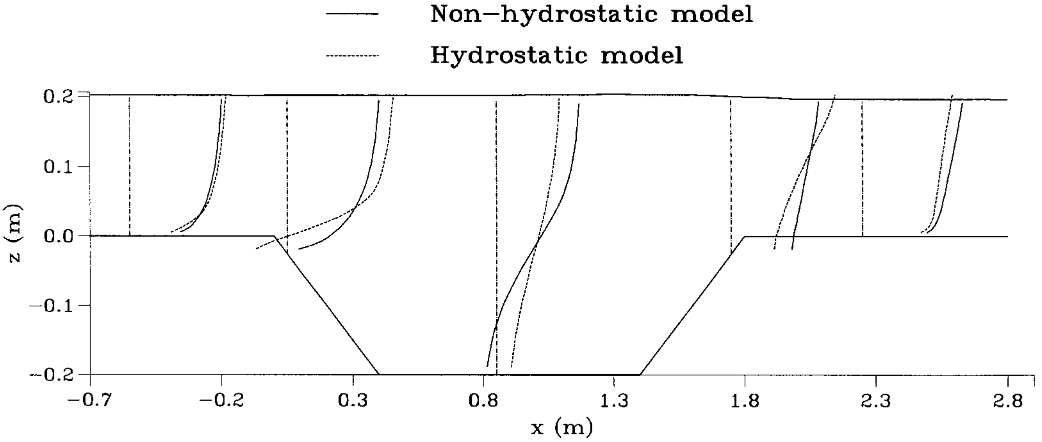

Figure 12. Comparison of velocity distributions.

$$\epsilon = c_\mu \frac{k^{1.5}}{0.09h}, \tag{99}$$

where the $\kappa = 0.4$ is the von Kármán constant.

4.2. Outflow boundary

At outflow, η is defined and zero normal gradients are specified for all the other variables.

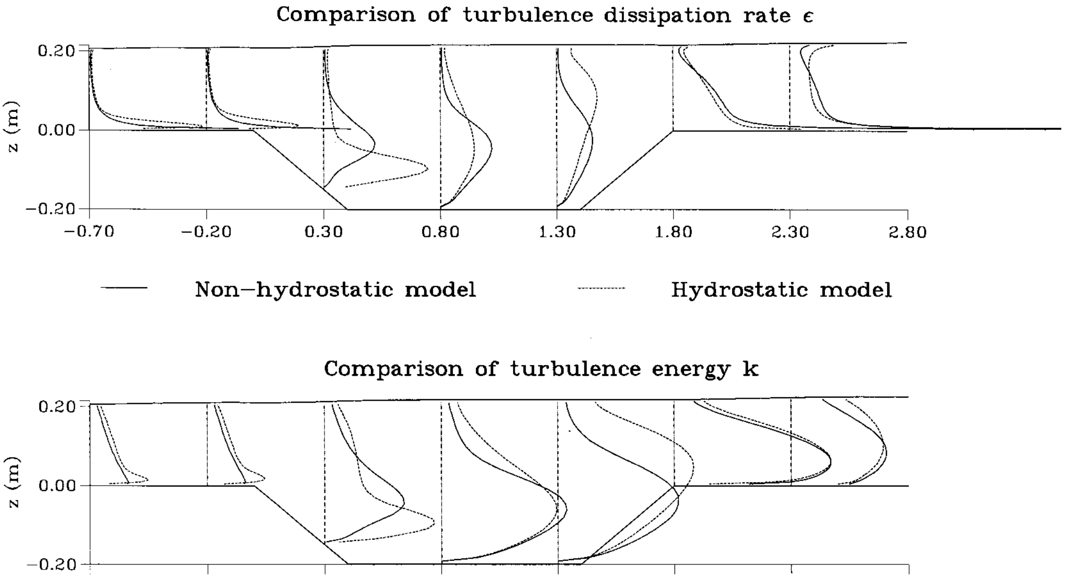

Figure 13. Comparisons of turbulence energy and dissipation rate.

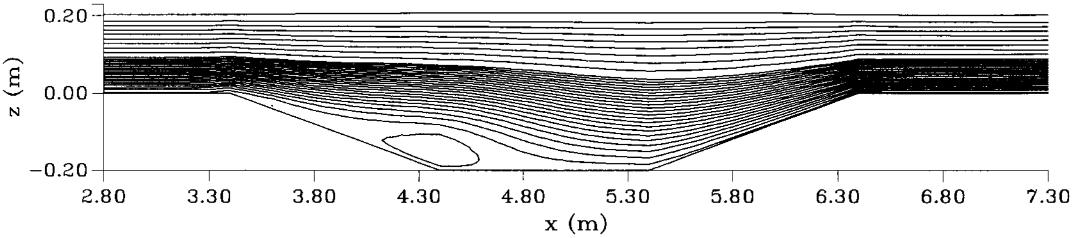

Figure 14. Streamlines for trench slope 1:5 with non-hydrostatic pressure.

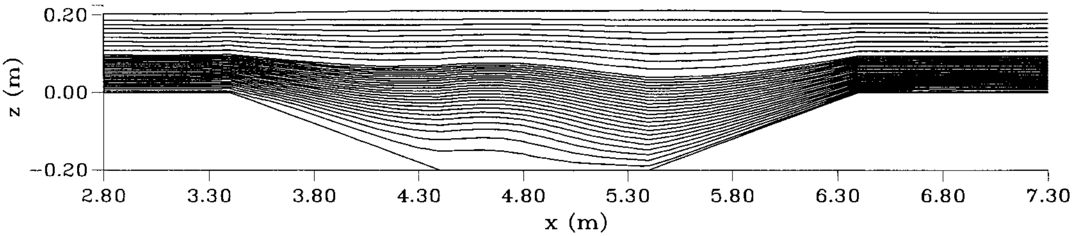

Figure 15. Streamlines for trench slope 1:5 with hydrostatic pressure.

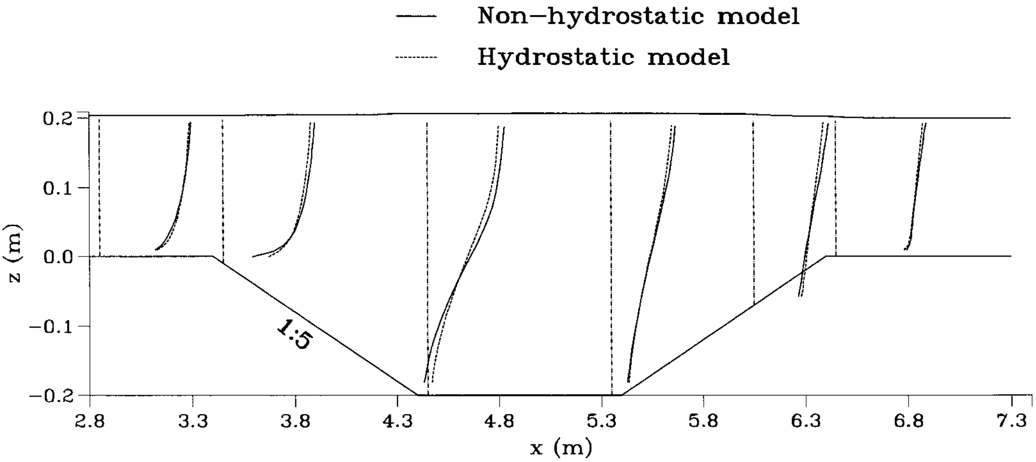

Figure 16. Comparison of velocity distribution for trench slope 1:5.

5. RESULTS

Detailed experimental data for testing the solver are limited. However, the case of steady current flow over a trench is an ideal case which was used for comparison with other numerical schemes [9,10]. The dimensions of the trench are shown in Figure 5. It has a rough bed with an equivalent roughness height, $k_s = 0.002$ m. The shear velocity V_* at inflow is deduced to be 0.033 m s^{-1} from the measured velocity profile, assuming $\kappa = 0.4$ [9]. The depth at outflow is 0.2 m.

Results are shown here with a mesh of 170 × 30 cells and, from comparisons with results from coarser meshes, are thought to be grid-independent. The numerical discretisation is defined by $\delta x = 0.1$ m, $\delta t = 0.002$ s and $a = 0.03$ in Equation (18), and a steady state was

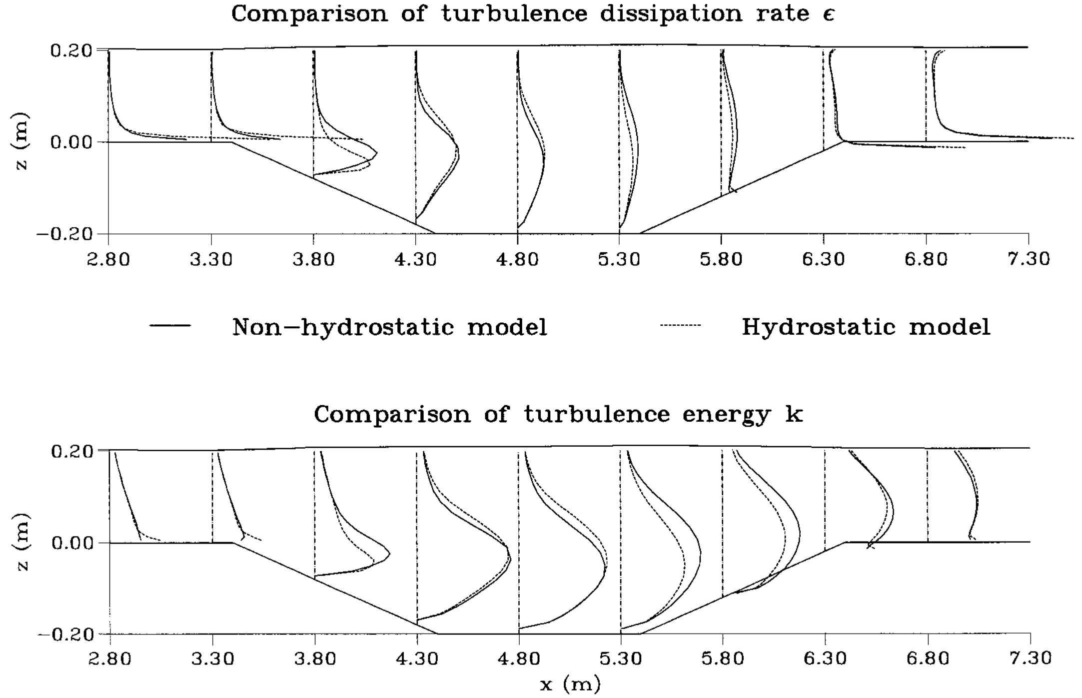

Figure 17. Comparisons of turbulence energy and dissipation rate for trench slope 1:5.

reached after ≈ 100 s. The inflow velocity and turbulence profiles are those for wide channel flow, given in Equations (92)–(95).

Figure 6 shows mean u velocity profiles at different points along the channel with experimental measurements. There is reasonable agreement, except for the profile just downstream of the upstream step where other numerical predictions (using the rigid-lid approximation) have also been weak. Figure 7 shows computed flow streamlines and it can be seen that separation does not occur precisely at the upstream step, which would be consistent with the larger velocity deficit in the experimental measurements. Figures 8 and 9 show profiles of kinetic energy k and shear stress τ_{xz} and again, agreement is similar to other numerical schemes. However, the limitations of turbulence predictions using such models is clearly demonstrated. Figure 10 shows the variation of bed shear stress along the channel and here agreement with experiment is rather better than other schemes, particularly close to the upstream and downstream steps. It seems likely that this is due to the incorporation of free-surface movement rather than the rigid-lid approximation.

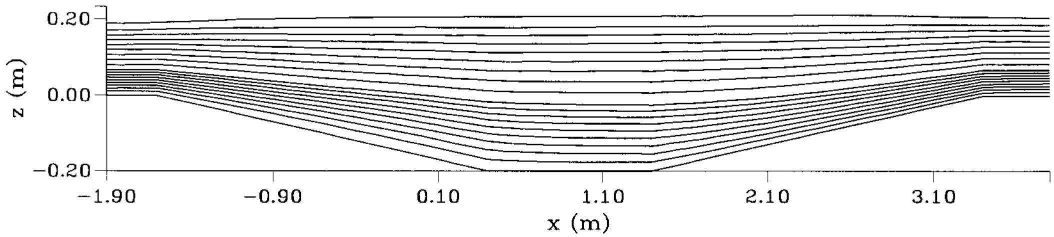

Figure 18. Streamlines for trench slope 1:10 with non-hydrostatic pressure.

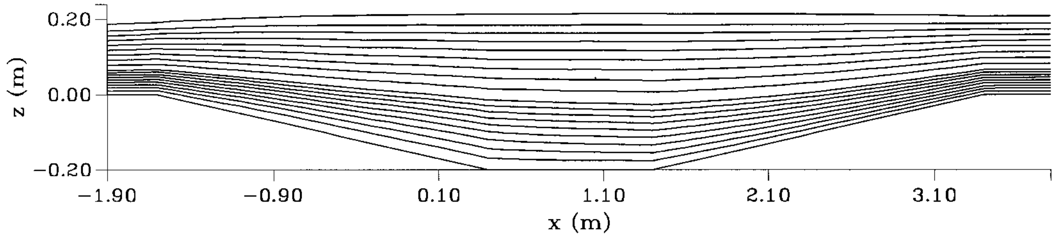

Figure 19. Streamlines for trench slope 1:10 with hydrostatic pressure.

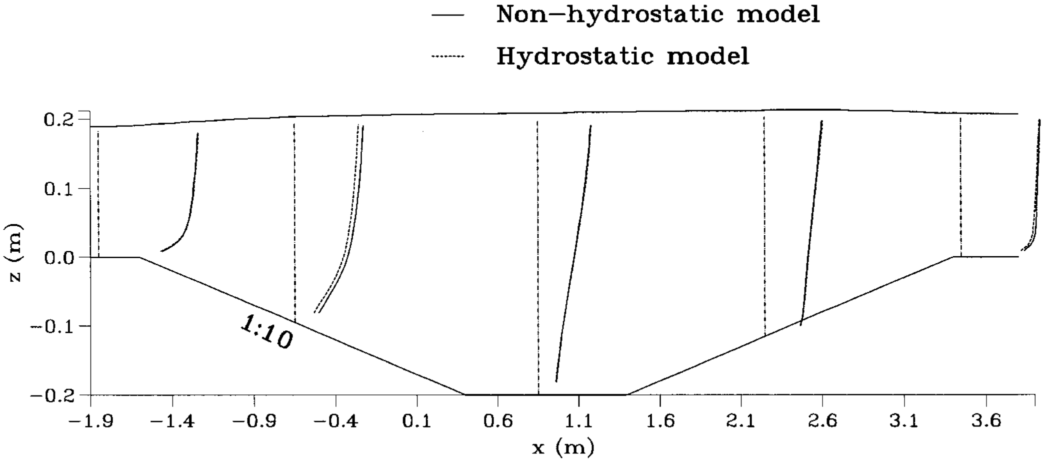

Figure 20. Comparison of velocity distributions for trench slope 1:10.

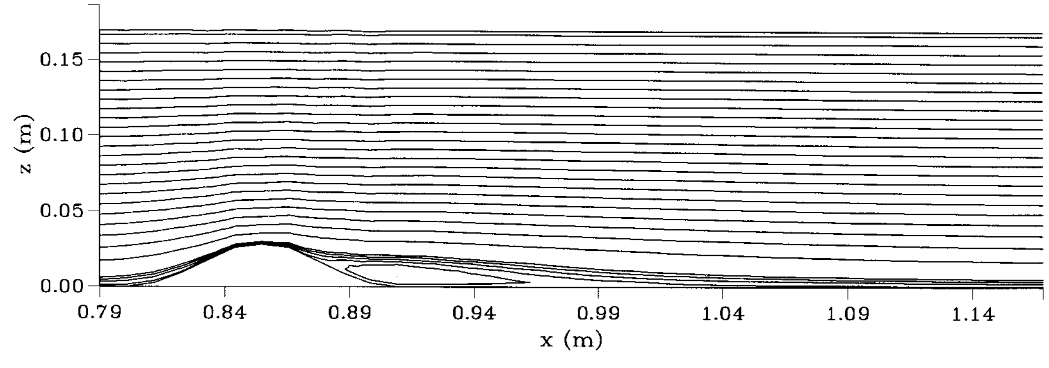

Figure 21. Streamlines for flow over mound with non-hydrostatic pressure.

The solver predicts the gross flow features, therefore, it is useful to run computations with the hydrostatic pressure assumption for different trench slopes, to determine the conditions where the non-hydrostatic pressure component becomes significant. First Figure 11 shows streamlines for the existing 1:2 slope trench and Figure 12 shows velocity profiles with and without non-hydrostatic pressure. While the separated region still occurs with the hydrostatic pressure alone, it is much smaller and the velocity profiles in Figure 12 are accordingly quite different. Figure 13 shows profiles of k and ϵ for completeness and the differences are quite substantial as would be expected. Figure 14 shows streamlines for a 1:5 slope trench with

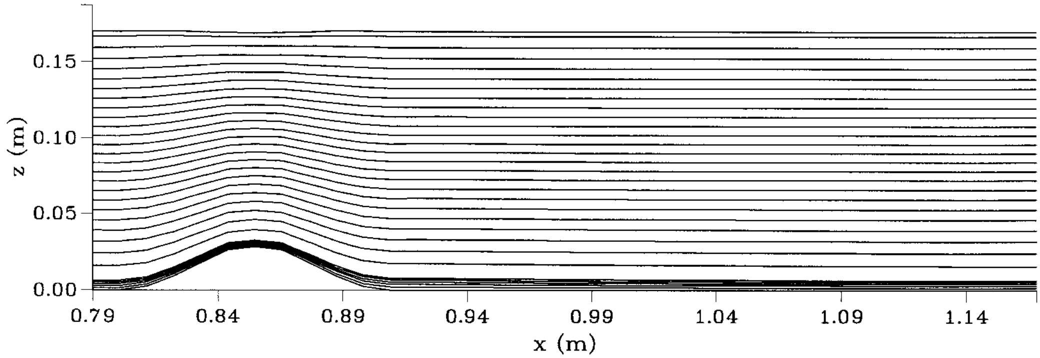

Figure 22. Streamlines for flow over mound with hydrostatic pressure.

non-hydrostatic pressure and Figure 15 with hydrostatic pressure only. A small separated region is seen with non-hydrostatic pressure but not without and the velocity profiles shown in Figure 16 are accordingly different, although the differences are now quite small. The k and ϵ profiles in Figure 17 show correspondingly much smaller differences. With the 1:10 slope trench the streamline patterns with and without non-hydrostatic pressure in Figures 18 and 19 are now very similar and the velocity profiles in Figure 20 are almost identical. k and ϵ profiles are correspondingly almost identical and are not shown.

It was considered desirable to also compute flow over a hump or mound with separation and some detailed water tunnel measurements are available in Reference [11] for a smooth surface. Unfortunately, the experimental velocity gives a high Froude number, which would cause the free surface to distort considerably from the horizontal surface representing the roof of the water tunnel. Nevertheless, the flow around such a mound was computed; where the largest slope is 45°, with a smaller upstream velocity (giving a nearly flat free surface) and homogeneous upstream turbulence conditions described in Equations (96)–(99). Figure 21 shows streamline plots with non-hydrostatic pressure and a separation bubble forms as it does in the experiments. The upstream separation point is slightly downstream of the experimental position but the length of the bubble is about the same. With hydrostatic pressure alone Figure 22 shows that the separation bubble does not form and this is reflected in the velocity profiles

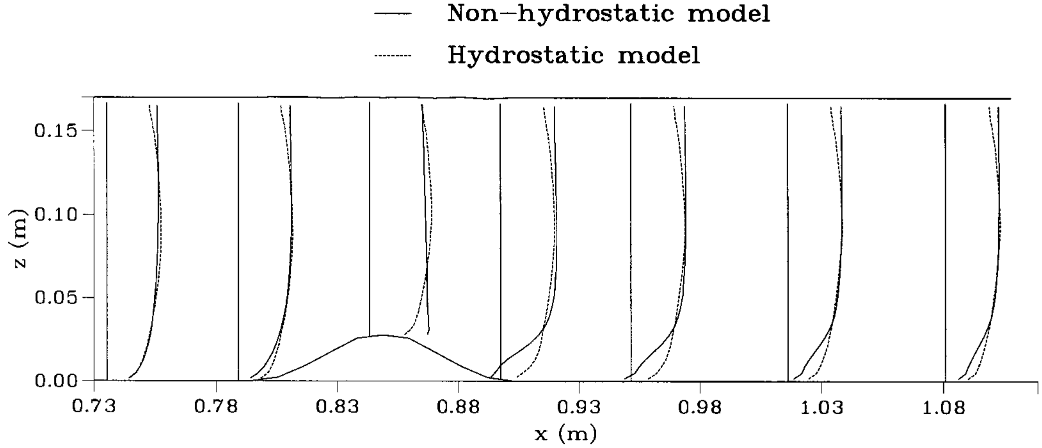

Figure 23. Comparison of velocity distributions.

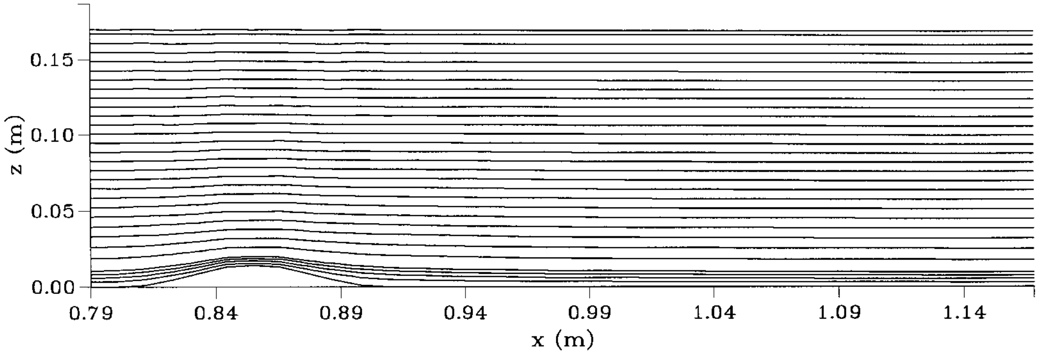

Figure 24. Streamlines for flow over smaller mound with non-hydrostatic pressure.

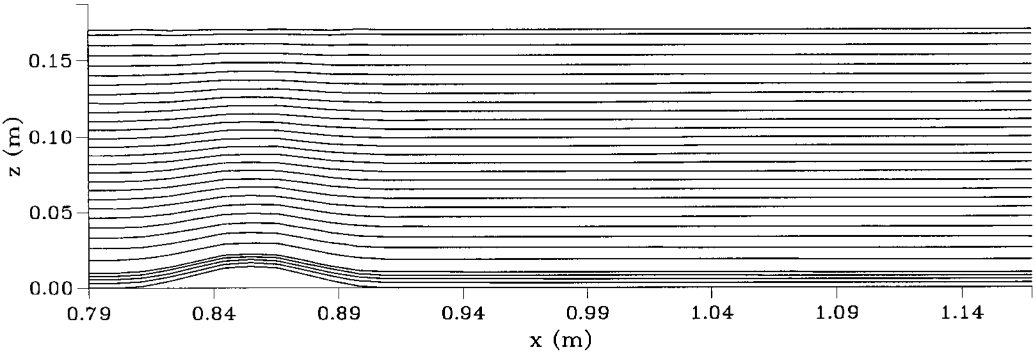

Figure 25. Streamlines for flow over smaller mound with hydrostatic pressure.

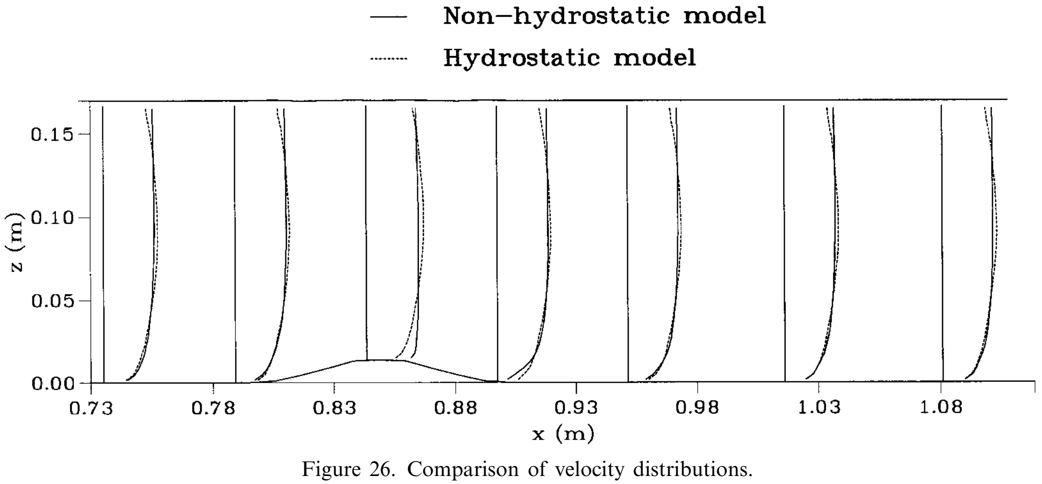

Figure 26. Comparison of velocity distributions.

shown in Figure 23. Flows were also computed for a mound of half the height and streamlines with and without non-hydrostatic pressure are shown in Figures 24 and 25. A separation bubble does not form in either case but now the velocity profiles shown in Figure 26 do show some distinct differences.

Results for unsteady problems will be shown in detail elsewhere. Satisfactory results have, in fact, been produced for the wave-maker problem (using second-order time stepping to minimise numerical dissipation) and a study of wave flows over rippled beds and bars is anticipated.

The method will be extended to three dimensions and detailed experiments for tidal flows around headlands with recirculations, being undertaken in the UK Coastal Research Facility [3], will be used for validation.

6. CONCLUSIONS

A numerical scheme for incorporating non-hydrostatic pressure in the shallow-water equations has been developed. This has been set up and tested for 2D vertical plane problems: the flow over a trench and over a mound. The method is based on the σ-co-ordinate system and $k-\epsilon$ turbulence modelling is incorporated. Reasonable agreement with experimental results is found in the trench problem, similar to previous computational studies which applied the rigid-lid, free-surface approximation and the same turbulence model. It is worth noting that more refined turbulence modelling produced little improvement for this problem [10]. Results with and without non-hydrostatic pressure were compared for the 1:2 slope trench investigated experimentally and also for 1:5 and 1:10 slope trenches, to test the validity of the usual hydrostatic pressure assumption. This was also done for the mound investigated experimentally and a shallower mound. As expected, separation zones were either not predicted or underpredicted in size, with the conventional hydrostatic pressure assumption which gave equivalent predictions only for the smallest slopes investigated.

The non-hydrostatic pressure solution is the most computationally expensive part of the scheme, although it is solved efficiently using a conjugate-gradient equation solver, and it may be restricted to parts of the flow where its influence is thought to be significant. In this way, the additional computational expense may be kept to a minimum. The method is being extended to 3D where these considerations are particularly significant.

ACKNOWLEDGMENTS

Funding from the UK EPSRC Grant GR/K95666 is gratefully acknowledged.

REFERENCES

1. P.K. Stansby, ‘Semi-implicit finite volume shallow-water flow and solute transport solver with $k-\epsilon$ turbulence model’, *Int. j. numer. methods fluids*, **25**, 285–313 (1997).
2. P.M. Lloyd and P.K. Stansby, ‘Shallow-water flow around conical islands of small side slope’, *J. Hydr. Eng., ASCE*, **123**, 1057–1077 (1997).
3. P.M. Lloyd, P.K. Stansby, D. Chen, J. Yin,Y. Chen and R.A. Falconer, ‘Oscillatory shallow-water flow around a conical headland’, Vol. 1, Theme B, *xxvii IAHR Congress*, San Francisco, 1997, pp. 791–796.
4. B. Johns, ‘The modelling of the free surface flow of water over topography’, *Coastal Eng.*, **15**, 257–278 (1991).
5. V. Casulli and G. Stelling, ‘Simulation of three-dimensional, non-hydrostatic free-surface flows for estuaries and coastal seas’, *Proc. Int. Conf. on Estuarine and Coastal Modeling*, ASCE, New York, NY, USA, 1996, p. 112.
6. V. Casulli and R.T. Cheng, ‘Semi-implicit finite difference methods for three-dimensional shallow water flow’, *Int. j. numer. methods fluids*, **15**, 629–648 (1992).
7. W. Rodi, *Turbulence Models and their Applications in Hydraulics*, 3rd edn., IAHR, Delft, The Netherlands, 1993.
8. G. Stelling and J.A.T.M. van Kester, ‘On the approximation of horizontal gradients in sigma co-ordinates for bathymetry with steep bottom slopes’, *Int. j. numer. methods fluids*, **18**, 915–935 (1994).
9. B.J. Alfrink and L.C. van Rijn, ‘Two-equation turbulence model for flow in trench’, *J. Hydraul. Eng. ASCE*, **109**, 941–958 (1983).

10. B. Basara and B.A. Younis, ‘Predictions of turbulent flows in dredged trenches’, *J. Hydraul. Res.*, **33**, 813–824 (1995).
11. G.P. Almeida, D.F.G. Durao and M.V. Heitor, ‘Wake flows behind two-dimensional model hills’, *Exp. Thermal Fluid Sci.*, **7**, 87–101 (1993).